nature nanotechnology

SUPPLEMENTARY INFORMATION

DOI: 10.1038/NNANO.2015.188

Characterization and manipulation of individual defects in hexagonal boron nitride using scanning tunnelling microscopy

Dillon Wong*, Jairo Velasco Jr.*, Long Ju*, Juwon Lee, Salman Kahn, Hsin-zon Tsai, Chad Germany, Takashi Taniguchi, Kenji Watanabe, Alex Zettl, Feng Wang and Michael F. Crommie

Table of Contents:

1. Comparison of Dot Intensities

The average dI/dV intensities for bright and dark dots in several of our maps cluster into distinct values, suggesting that both dot-defect types are located in multiple layers of the BN crystal. In Fig. S1b we illustrate our methodology for acquiring the average dI/dV intensity of dot-defects on an enlarged bright dot. The sampling area for an

average intensity is defined by the orange square (~ 49 nm^2), which encloses most of the bright dot. We used a similar sampling area throughout our analysis because it represents a balance between under and over sampling. Also, for each map, the boxed area was the same for each dot.

Fig. S2a and Fig. S2c are the same dI/dV maps, and they host bright and dark dots denoted by coloured circles in each map separately. Using the methodology described above, we acquired the average dI/dV intensities from the bright dots in Fig. S2a and plotted this in Fig. S2b. We carried out the same procedure for the dark dots in Fig. S2c and plotted their average intensities in Fig. S2d. We find that the dot defects cluster into distinct values within the error bar, which is half of the moiré amplitude. For each of the bright and dark dots we observe three unambiguous values for the average dI/dV intensity. Subsequent dI/dV maps that focus on dots at different locations show a similar trend of clustering at distinct average intensity values. The number of these values varies from two to five. We believe the observed clustering of the average dI/dV intensities into distinct values provides evidence that the dot-defects are located in distinctly different BN layers.

In Fig. S3 we compare the bright dots from different dI/dV maps by using a histogram. First, to eliminate tip density of states prefactors, we define normalized dot intensities by dividing the average dI/dV intensity of each dot by the average dI/dV intensity of the brightest dot from its respective dI/dV map. This was performed for 56 bright dots. The histogram shows that the normalized dot intensities from different maps cluster into three groups of normalized intensities, which we denote with three different

colours. The observed clustering provides evidence that the dot-defects are located in distinct BN layers.

2. Defect Densities

The defect densities in our dI/dV maps are consistent with the charge inhomogeneity seen in transport measurements of high quality graphene/BN heterostructure devices. By counting the number of defects visible in several dI/dV maps across three different devices, we found defect densities in the range of 10^{10} - 10^{9} cm^{-2}. In transport measurements, the charge inhomogeneity can be extracted from the full width at half maximum of highly symmetric $R(V_g)$ curves (R is the measured resistance and V_g is the gate voltage responsible for the electrostatic induced charge density in graphene). Previous transport studies[1,2] report charge inhomogeneities in the range of 10^{10} - 10^{9} cm^{-2}. The agreement between the two distinct measurement techniques indicates that these defects are likely a limiting factor for mobility in graphene/BN devices.

3. Pristine Graphene Lattice

In order to verify that the dots and rings are not caused by adatoms, defects in the graphene lattice (e.g. vacancies and substitutional atoms), or atoms and molecules trapped between graphene and BN, we acquired atomically resolved topographic images in regions inhabited by dots and rings. An example of such a topographic image is shown in Fig. S4, which clearly displays a perfectly periodic graphene lattice superimposed on a moiré pattern at the same location as a defect. Since the moiré pattern arises from an interlayer interaction between the graphene monolayer and BN, atoms and molecules

trapped underneath graphene should disrupt the moiré periodicity. No such distortions in the moiré pattern are observed. Furthermore, there have been many STM studies involving adsorbates on graphene and lattice defects in graphene. Brar *et al*., Wang *et al*., and Eelbo *et al*. studied metal adatoms (Co, Ca, Fe, and Ni) on graphene[3-6]. Balog *et al*. and Scheffler *et al*. studied hydrogen adatoms on graphene[7,8], Zhao *et al*. studied nitrogen and boron substitutional defects in graphene[9,10], and Ugeda *et al*. studied vacancies in graphene[11]. In all of these studies, the adatoms and graphene lattice defects were clearly visible in STM topographic data. No such topographic features were observed for the dots and rings presented in this paper. We conclude that the dots and rings originate from defects in BN.

4. Tip Height Dependence of d*I*/d*V* and Defect Charge Determination

The charge of a defect seen by STM cannot be determined from an individual d*I*/d*V* map since it does not contain enough information. The d*I*/d*V* maps must be supplemented with energy-dependent d*I*/d*V* spectroscopy[5,6].

First, we explain what a d*I*/d*V* map represents. Since d*I*/d*V* is proportional to the electronic LDOS[12], a dI/d*V* map is a measure of LDOS(x,y,z,E). Here, we define x and y as parallel to the surface, z as perpendicular to the surface, and E as energy. As an STM raster scans across a surface, the STM tip height z does not remain at a constant height above atomic nuclei. Since wave functions decay exponentially into the vacuum,

$$\mathrm{LDOS}(x, y, z, E) = \mathrm{LDOS}(x, y, z_0, E) e^{-\frac{(z - z_0)}{\lambda}}$$

where z_0 is a constant height over atomic nuclei, λ characterizes the length scale of the exponential decay, and z - z_o denotes vertical excursions from the plane defined by z_o.

Because STM measurements are performed with a constant-current I_o feedback condition, the following condition holds:

$$I_0 \propto \int_0^{V_S} \mathrm{LDOS}(x, y, z, E_F + eV) dV \propto e^{-\frac{(z-z_0)}{\lambda}} \int_0^{V_S} \mathrm{LDOS}(x, y, z_0, E_F + eV) dV$$

Solving for the exponential tip height factor (which we call γ):

$$\gamma = e^{-\frac{(z-z_0)}{\lambda}} \propto \frac{1}{\left| \int_0^{V_S} \mathrm{LDOS}(x, y, z_0, E_F + eV) dV \right|}$$

This means that

$$\frac{dI}{dV}(x, y, z)\Big|_{V=V_s} \propto \mathrm{LDOS}(x, y, z, E_F + eV_s) \propto \frac{\mathrm{LDOS}(x, y, z_0, E_F + eV_s)}{\left| \int_0^{V_s} \mathrm{LDOS}(x, y, z_0, E_F + eV') dV' \right|}$$

Thus, a dI/dV map is not a perfect representation of LDOS at energy $E_F + eV_s$ and fixed height z_0 (for more details, see Wittneven *et al.*[13]). Rather, dI/dV maps also include information about LDOS at energies between E_F and $E_F + eV_s$. For this reason, energy-dependent dI/dV spectroscopy must be acquired to determine a dot's charge sign. This is demonstrated by the dI/dV spectra for both types of dots shown in Figs. 2c and 2d of the main text. Since the initial tunnelling parameters (I_0 = 0.4 nA, V_s = -0.5 V) are the same for every dI/dV curve, there must also be the same area underneath each curve from V_s = -0.5 V to V_s = 0 V. Due to the constant-current feedback condition, the tip height z is adjusted such that each dI/dV curve is naturally multiplied in the bare data by a γ factor that ensures $I_0 = \left| \int_0^{V_s} \frac{dI}{dV} dV \right|$.

Each curve in Figs 2c and 2d of the main text is thus naturally multiplied by a different γ factor to ensure the constant-current feedback condition $I_0 = \left|\int_0^{V_s} \frac{dI}{dV} dV\right|$. This must be considered when dI/dV values at different locations are compared. One way to do this is to compare ratios of dI/dV values at different energies on the same curve. Here it is useful to define the following asymmetry factor:

$$\text{Asymmetry Factor} = \frac{\left.\frac{dI}{dV}\right|_{V_s=+0.5V}}{\left.\frac{dI}{dV}\right|_{V_s=-0.5V}}$$

The exponential tip height factor is removed in such a ratio, and values of the asymmetry factor at different spatial locations can be meaningfully compared independent of the initial tunnelling conditions. In Fig. S5, we plot the asymmetry factor against distance from the centre of the bright and dark dots shown in Figs 2a and 2b of the main text. For a positively charged defect in BN (what we call a "bright" dot), the asymmetry factor decreases with distance because a positively charged defect attracts electron-like Dirac fermions and repels hole-like Dirac fermions. This trend is reversed for negatively charged defects (what we call "dark" dots), for which the asymmetry factor increases with distance from the dot centre. Wang *et al*. originally developed this asymmetry analysis for studying charged adatoms on graphene[5,6].

The initial tunnelling bias for the spectroscopy shown in Fig. 2c,d of the main text was negative. If we change the initial tunnelling bias to V_S = +0.5 V, this fixes the area under the dI/dV curves over the range $0 \leq Vs \leq +0.5$V. This data is shown for both a positively charged and a negatively charged defect in Fig. S6a and Fig. S6b, respectively. Notice that the left sides of the dI/dV curves in Fig. 2 of the main text all align, while the

right sides of the dI/dV curves in Fig. S6 all align. Whether the left sides or right sides of dI/dV align depends simply on the sign of the initial tunnelling bias and does not affect our determination of impurity charge. This can be rationalized as follows: The states below the Dirac point represent hole-like charge carriers. Thus, dI/dV in Fig. S6a decreases near the positive defect because holes are repelled. Likewise, dI/dV in Fig. S6b increases near the negative defect because holes are attracted. Thus, it is possible to determine the defect charge type regardless of the choice of sign for the initial tunnelling bias.

5. Determination of the Charge Sign of a Ring

The charge state of the ring shown in Fig. 3 of the main text can be determined through dI/dV spectroscopy similar to the bright and dark dots. As seen in the figure, the ring is closed at V_g = +30 V, and is charged when the STM tip lies outside of the ring. Fig. S7 shows dI/dV spectra for various distances outside of the ring. Analysis similar to that described in the previous section reveals that the ring represents a negatively charged defect. This is consistent with the fact that the bright ring in Fig. 3a of the main text is surrounded by a dark cloud. This dark cloud is equivalent to a dark dot, indicating that the defect associated with the ring is negatively charged when the tip is outside the bright ring structure.

6. Additional Details Regarding Theoretical Explanation of the Ring Defect

Here we present additional details for our description of the ring phenomenon that incorporates a defect in the topmost layer of BN. Fig. 3d of the main text depicts the local electronic structure of the graphene immediately above a negatively charged defect when

the lateral tip-to-defect distance r is large. The electric potential of the tip relative to graphene is $V_{tip} = -V_s + (\Phi_{graphene} - \Phi_{PtIr})/e$, with graphene work function $\Phi_{graphene} \approx 4.5$ eV[14] and platinum-iridium work function $\Phi_{PtIr} \approx 5.2$ eV[15]. The tip is capacitively coupled to the graphene directly above the defect through the equation $|e|\delta n = C(r)V_{tip}$, where δn is the local change in graphene electron density and $C(r)$ is a capacitance that increases with decreasing r. For the dI/dV maps in Figs 3a and 3b of the main text, $V_{tip} < 0$, so the electrostatic gating from the tip lowers the electron density of the graphene directly beneath the tip. Thus, as the tip approaches the defect, $C(r)$ increases and δn becomes more negative. Eventually, the Fermi energy crosses the defect level when the tip is at some distance R away from the defect (where R is the ring radius). Fig. 3e of the main text shows that for $r < R$, the Fermi energy is below the defect level, and the defect is neutralized. Since the charge state of the defect (and hence, the LDOS in graphene) is different for the two conditions $r > R$ and $r < R$, there is an abrupt change in the tunnelling current at $r = R$. In a dI/dV map, this manifests as a ring with radius R separating the region where the tip is too far to neutralize the defect ($r > R$) from the region where the tip is close enough to neutralize the defect ($r < R$).

This model is in agreement with the experimental data shown in Fig. 3c of the main text. For a fixed V_s and starting with the graphene Fermi energy above the defect energy level, the ring radius R increases with decreasing V_g until a critical back-gate voltage $V_c = 6 \pm 1$V, upon which the ring vanishes (as $R \rightarrow \infty$). This can be explained if V_c is the back-gate voltage that causes the Fermi energy to align with the defect energy level. As V_g approaches V_c from above, the $|\delta n|$ required to neutralize the defect decreases, so R increases. The experimental value of V_c depends on the local charge

neutrality point, which varies due to charge inhomogeneity, but dI/dV spectroscopy reveals that V_c corresponds to a Fermi energy (and defect level) 30 ± 10 meV above the Dirac point. In addition, Fig. 3c of the main text shows that (at fixed V_g) the ring radius decreases as V_s approaches -800 mV. This is expected from the equation $C(R) = |e|\delta n/V_{tip}$, since V_{tip} approaches zero as V_s approaches $\Phi_{graphene} - \Phi_{PtIr} = -750 \pm 50$ meV. As $|V_{tip}|$ decreases, $C(R)$ increases, leading to a smaller ring radius R.

A more detailed analysis of the data in Fig. 3c of the main text can be performed. Since $C(R) = |e|\delta n/V_{tip}$ is only a function of R, the data can be rescaled onto a single curve. Fig. S8a shows $|V_g\text{-}V_c|/|\text{-}V_s + (\Phi_{graphene} - \Phi_{PtIr})/e|$ plotted against ring radius R, where $V_c = 6$ V and $\Phi_{graphene} - \Phi_{PtIr} = -0.8$ eV, as expected from the previous discussion. The data all collapses onto a single curve independent of sample bias V_s. Furthermore, the curve follows a shifted power law

$$\frac{V_g - V_c}{|-V_s + (\Phi_{\mathrm{graphene}} - \Phi_{\mathrm{PtIr}})/e|} = \frac{\alpha}{(R^2 + \beta^2)^{\gamma}}$$

where α, β, and γ are geometric factors that depend on the tip and sample geometry. Fig. S8b plots $(|V_g\text{-}V_c|/|\text{-}V_s + (\Phi_{graphene} - \Phi_{PtIr})/e|)^{-1/\gamma}$ as a function of R^2, using $\gamma = 0.63$. The data in Fig. S8b falls onto a straight line, indicating that the above shifted power law function is a good fit for the data in Fig. S8a.

If the tip was an infinite plane parallel to the graphene, $\gamma = 0$ (because there would be no R dependence). On the other hand, if the tip was a perfect sphere (and graphene was perfectly metallic), $\gamma = 1$. Our value of $\gamma = 0.63$ reflects a tip geometry somewhere "in between" a plane and a sphere.

7. Gate Dependence of d*I*/d*V*

Here we examine the effect of gate voltage on the dot defects. Figs S9a,b show d*I*/d*V* spectroscopy measured at different distances away from the bright and dark dots shown in Fig. 2 of the main text, but at a different gate voltage of V_g = 5 V. These spectroscopy curves look similar to the V_g = 20 V data from Fig. 2, except for a shifted Dirac point. More illuminating information can be obtained from Figs S9c,d, which show d*I*/d*V* maps (V_s = -0.30, I = 0.4 nA) of two bright dots and one dark dot at V_g = 5 V and V_g = -15 V, respectively. All three dots are present in both d*I*/d*V* maps, but the dot defects in the V_g = -15 V map appear to be laterally smaller than in the V_g = 5 V map. This represents a decrease in graphene's screening length with increasing charge carrier density. The Thomas-Fermi screening length is given by [16]

$$\lambda_{TF} = \frac{\pi \epsilon_0 \kappa \kappa^* \hbar v_F}{e^2 k_F}$$

where k_F is the magnitude of the Fermi wave vector, v_F is the Fermi velocity, κ is the substrate dielectric constant, and κ* is the interband dielectric constant. Increasing the gate voltage $|V_g - V_{CNP}|$ also increases k_F, reducing λ_{TF}. Thus, the dot defects appear smaller at the higher magnitude gate voltage. We emphasize that this reflects a change in the graphene layer's screening properties and does not reflect any actual change in the properties of the BN defects.

8. Procedure for Defect Manipulation

The procedure for applying tip pulses to manipulate defects in a BN crystal substrate is presented below:

1. Set V_s = 0.5 V, V_g = 0 V, and I = 0.4 nA under closed loop conditions.
2. Turn off STM feedback loop.
3. Withdraw the STM tip 1 nm away from set point position.
4. Ramp V_s up to +5 V over a period of 30 seconds.
5. Wait Δt = 10 seconds. This wait time can be varied.
6. Decrease V_s back to 0.5 V over a period of 30 seconds.
7. Turn on STM feedback loop.

9. Discussion of Possible Models for Defect Manipulation

Direct tunnelling[17], phonon-assisted tunnelling[18], and the Poole-Frenkel effect[19] are electric-field-induced charge emission mechanisms that can explain the charge exchange between defects that we observe in our experiment. Previous studies of these mechanisms have determined that the defect emission rate W can be written as

$$W \propto e^{\beta E^{\gamma}}$$

where E is the magnitude of the applied electric field, γ is an exponent that depends on the particular mechanism, and β is a coefficient that may depend on temperature**.** This relation shows that charge emission mechanisms are acutely sensitive to E. In our experiment, we found that charge exchange between defects had a sharp tip-to-sample voltage threshold of $V_s \approx 3$V for the tip-pulse procedure described above (step 4 in Section 7). This is consistent with the expected E dependence of the three charge emission mechanisms mentioned above, although each has a distinct E and temperature dependence[20]. Future experiments employing wide temperature and electric field

tunability will be useful for pinpointing the precise mechanism responsible for observed defect charge exchange.

10. Defect Manipulation Video

This movie consists of dI/dV maps (similar to Fig. 4 of the main text) and shows dot-defect manipulation for each map. The manipulation is generated by carrying out the defect manipulation procedure outlined above in Section 8.

11. STM Tip Navigation to Graphene

Since insulators do not support a tunnelling current for normal STM operation, our tip must be safely navigated to the graphene device without crashing into either SiO_2 or BN. For sample sizes larger than 30 x 30 μm^2, the STM tip is coarse aligned with graphene/BN (using a stick-slip piezoelectric actuator with a range of a few millimetres) at liquid helium temperature with the assistance of a long-distance optical microscope (Model K2 from Infinity Photo-Optical Company). Although our optical microscope setup has a field of view large enough to image a centimetre-sized SiO_2 chip, it is not able to resolve features smaller than 30 x 30 μm^2. To locate these smaller graphene devices, we employ a scanning gate technique[21] in which the graphene conductance is monitored while moving the tip laterally. The tip ($V_s = \pm 10$ V) electrostatically gates the graphene, and we measure a change in the conductance when the tip is directly above the graphene (compared to when the tip is not above graphene). To maximize the conductance change, the tip is placed as close to the surface as possible without crashing. This can be accomplished by approaching a grounded metal electrode near graphene. Additionally, the back-gate voltage is set such that the rate of change of the conductance $G(V_g)$ is maximal. The observed conductance change depends on the sample size (with smaller

samples showing greater conductance changes) and the tip geometry, but a 5% change is not unreasonable for most graphene devices. If executed correctly, this technique allows reliable navigation of the tip to the graphene without risk of crashing. A detailed step-by-step procedure is presented below:

1. Approach the source or drain electrode of the graphene/BN device using a coarse piezoelectric motor and a long range optical microscope.
2. Retract the STM tip from the electrode by a "safe" distance. What is considered "safe" depends on how parallel the coarse motion is with respect to the sample stage, which can vary depending on the STM and sample mounting procedure. It requires some trial and error to determine typical "safe" distances for each setup.
3. Change the bias to $V_s = \pm 10$ V. Measure $G(V_g)$, and set V_g such that dG/dV_g is a maximum.
4. Walk the STM tip towards the graphene while monitoring the conductance G. Place the tip in the position where G deflects most from the background value.
5. Walk the STM tip in a perpendicular direction while monitoring G. Place the tip in the position where G deflects most from the background value.
6. Iterate steps 4 and 5 until the STM tip converges on the graphene/BN device position.
7. Approach and scan graphene.

1. Young, A.F. Dissertations, Columbia (2012).
2. Amet, F., Williams, J.R., Watanabe, K., Taniguchi, T. & Goldhaber-Gordon, D. Insulating Behavior at the Neutrality Point in Single-Layer Graphene. *Physical Review Letters* **110**, 216601 (2013).
3. Eelbo, T. *et al.* Adatoms and Clusters of 3d Transition Metals on Graphene: Electronic and Magnetic Configurations. *Physical Review Letters* **110**, 136804 (2013).
4. Brar, V.W. *et al.* Gate-controlled ionization and screening of cobalt adatoms on a graphene surface. *Nature Phys.* **7**, 43-47 (2011).
5. Wang, Y. *et al.* Mapping Dirac quasiparticles near a single Coulomb impurity on graphene. *Nature Phys.* **8**, 653-657 (2012).
6. Wang, Y. *et al.* Observing Atomic Collapse Resonances in Artificial Nuclei on Graphene. *Science* **340**, 734-737 (2013).
7. Scheffler, M. *et al.* Probing Local Hydrogen Impurities in Quasi-Free-Standing Graphene. *ACS Nano* **6**, 10590-10597 (2012).
8. Balog, R. *et al.* Atomic Hydrogen Adsorbate Structures on Graphene. *Journal of the American Chemical Society* **131**, 8744-8745 (2009).
9. Zhao, L. *et al.* Visualizing Individual Nitrogen Dopants in Monolayer Graphene. *Science* **333**, 999-1003 (2011).
10. Zhao, L. *et al.* Local Atomic and Electronic Structure of Boron Chemical Doping in Monolayer Graphene. *Nano Letters* **13**, 4659-4665 (2013).
11. Ugeda, M.M., Brihuega, I., Guinea, F. & Gómez-Rodríguez, J.M. Missing Atom as a Source of Carbon Magnetism. *Physical Review Letters* **104**, 096804 (2010).
12. Tersoff, J. & Hamann, D.R. Theory of the scanning tunneling microscope. *Physical Review B* **31**, 805-813 (1985).
13. Wittneven, C., Dombrowski, R., Morgenstern, M. & Wiesendanger, R. Scattering States of Ionized Dopants Probed by Low Temperature Scanning Tunneling Spectroscopy. *Physical Review Letters* **81**, 5616-5619 (1998).
14. Yu, Y.-J. *et al.* Tuning the Graphene Work Function by Electric Field Effect. *Nano Letters* **9**, 3430-3434 (2009).
15. Zhou, S. *et al.* Rectifying behaviors of Langmuir–Blodgett films of an asymmetrically substituted phthalocyanine. *Chemical Physics Letters* **297**, 77-82 (1998).
16. Hwang, E.H. & Sarma, S.D. Dielectric function, screening, and plasmons in 2D graphene. *cond-mat/0610561*.
17. Simmons, J.G. Generalized Formula for the Electric Tunnel Effect between Similar Electrodes Separated by a Thin Insulating Film. *Journal of Applied Physics* **34**, 1793-1803 (1963).
18. Makram-Ebeid, S. & Lannoo, M. Quantum model for phonon-assisted tunnel ionization of deep levels in a semiconductor. *Physical Review B* **25**, 6406-6424 (1982).
19. Frenkel, J. On Pre-Breakdown Phenomena in Insulators and Electronic Semi-Conductors. *Physical Review* **54**, 647-648 (1938).
20. Ganichev, S.D. *et al.* Distinction between the Poole-Frenkel and tunneling models of electric-field-stimulated carrier emission from deep levels in semiconductors. *Physical Review B* **61**, 10361-10365 (2000).
21. Xue, J. Dissertations The University of Arizona (2012).

Supplementary Figure S1: d*I*/d*V* map of bright and dark dots and methodology of dot intensity analysis. (a) d*I*/d*V* map (I = 0.4 nA, V_s = -0.25 V) of graphene/BN shows various dot and ring defects. (b) The orange box shows typical dot intensity sampling area where a balance between over and under sampling of d*I*/d*V* intensity is achieved.

Supplementary Figure S2: **d*I*/d*V* map showing bright and dark dots intensity distribution.** (a) and (c) both show the same d*I*/d*V* map (I = 0.4 nA, V_s = -0.25 V) of graphene/BN exhibiting bright and dark dot defects. Coloured circles denote intensity of dots (same colour used for same intensity); bright dots circled in (a), and dark dots circled in (c). (b) and (d) the average d*I*/d*V* intensity is plotted for bright and dark dots, respectively. The error bar represents ± (moiré amplitude/2). The bright and dark dots each cluster into distinct values in this image.

Supplementary Figure S3: **Histogram of normalized d*I*/d*V* dot-defect intensities**. 56 object histogram of normalized bright dot d*I*/d*V* intensities from several d*I*/d*V* maps. The bright dots cluster into three normalized dot intensities. We denote these clusters with three different colours.

Supplementary Figure S4: **Atomically resolved lattice for graphene/BN.** STM topographic images show that the dots and rings do not distort the moiré superlattice. Location of a ring defect originating from the underlying BN insulator is centred at the cross hair (tunnelling parameters: I = 0.4 nA, V_s = -0.1 V).

Supplementary Figure S5: **Asymmetry factor vs. distance from dot centre.** The asymmetry factor derived from d*I*/d*V* spectra obtained as a function of distance from dot defect centre decreases with increasing distance from a positive ("bright") dot centre and increases away from a negative ("dark") dot centre. (Dashed lines are guide to the eye).

Supplementary Figure S6: **Spatially dependent d*I*/d*V* spectroscopy.** (a-b) (a) d*I*/d*V* spectroscopy (initial tunnelling parameters: I = 0.4 nA, V_s = +0.5 V, V_g = 20 V) measured on graphene at different lateral distances from the centre of the bright dot in Fig. 2 of the main text. (b) Same as (a), but for the dark dot. With the initial tunnelling bias V_s=+0.5 the areas under the dI/dV curves for $0 \leq V_s \leq +0.5$V are fixed, in contrast to Fig. 2 of the main text. The charge polarity of dot defects can be determined in a similar manner regardless of the sign of the initial tunnelling parameters.

Supplementary Figure S7: **Spatially dependent d*I*/d*V* spectroscopy near ring defect.** d*I*/d*V* spectroscopy (initial tunnelling set point: V_S = -0.5 V, I = 0.4 nA, V_g = 30 V) as a function of distance from the centre (and outside) of a closed ring (same region as Fig. 3 of the main text). Asymmetry trend shows that the ring corresponds to a negatively charged.

Supplementary Figure S8: **Relationship between the gate voltage and tip electrostatic potential.** (a) In agreement with our model, the data in Fig. 3c of the main text collapses onto a single curve after dividing by the tip electrostatic potential. This is

proportional to the capacitance between the tip and the graphene above the ring defect as a function of tip-defect distance. (b) The capacitance obeys a simple shifted power law for γ=0.63.

Supplementary Figure S9: **Gate dependence of d*I*/d*V* spectra and maps.** (a) d*I*/d*V* spectroscopy (initial tunnelling parameters: I = 0.4 nA, V_s = +0.5 V, V_g = 5 V) measured on graphene at different lateral distances from the centre of the bright dot in Fig. 2 of the main text. (b) Same as (a), but for the dark dot. (c) d*I*/d*V* map (V_s = -0.30, I = 0.4 nA, V_g = 5 V) containing three dot defects. (d) Same as (c), but for V_g = -15 V.

Supplementary Figure S1

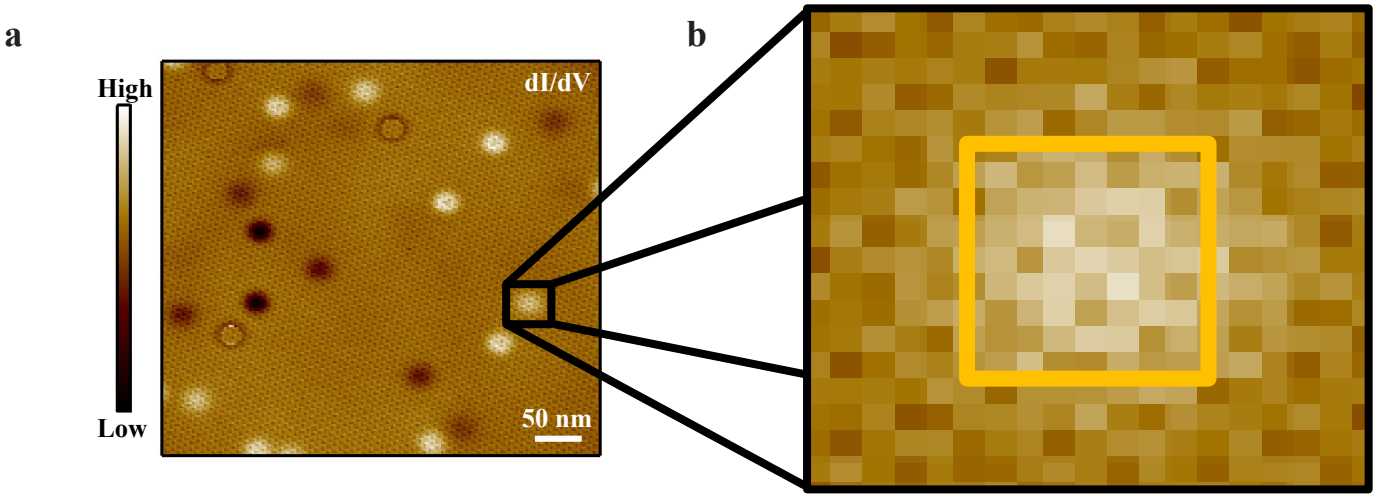

Supplementary Figure S2

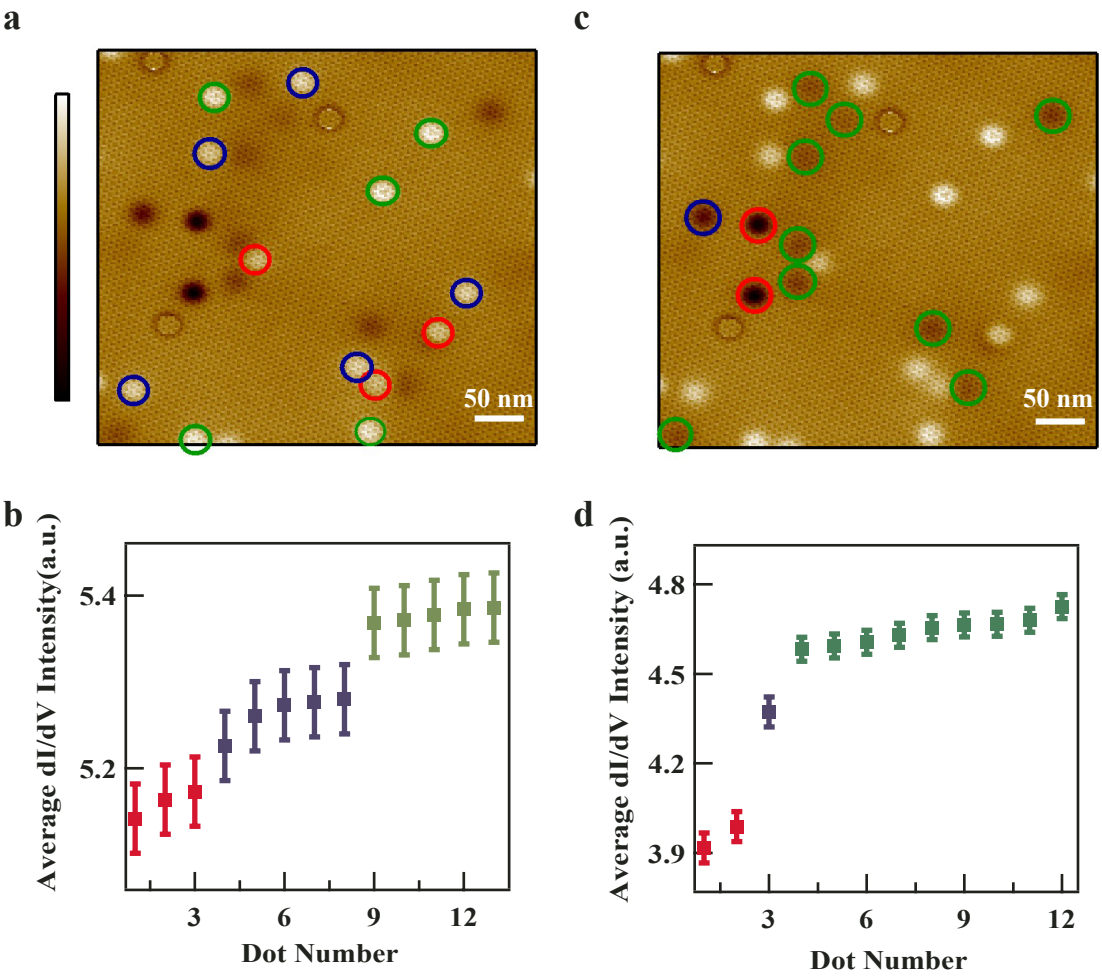

Supplementary Figure S3

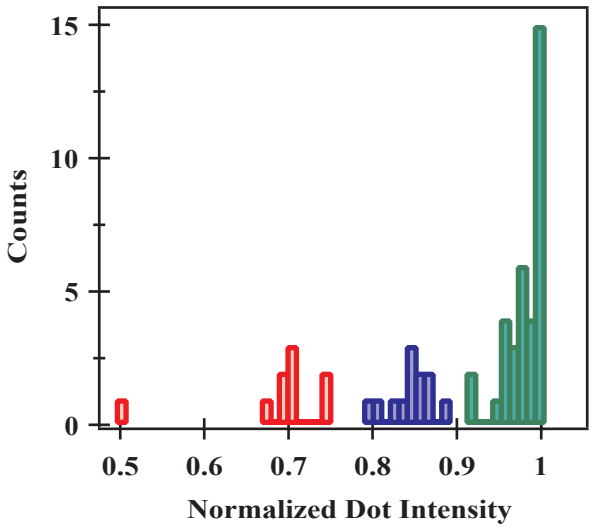

Supplementary Figure S4

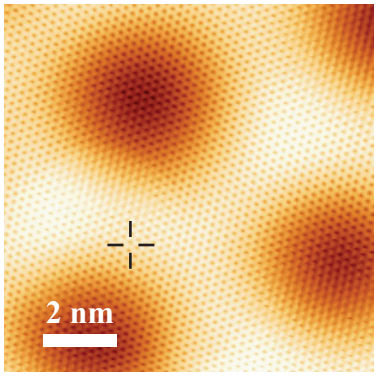

Supplementary Figure S5

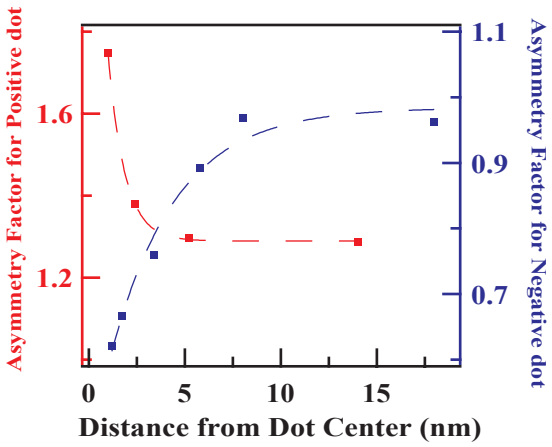

Supplementary Figure S6

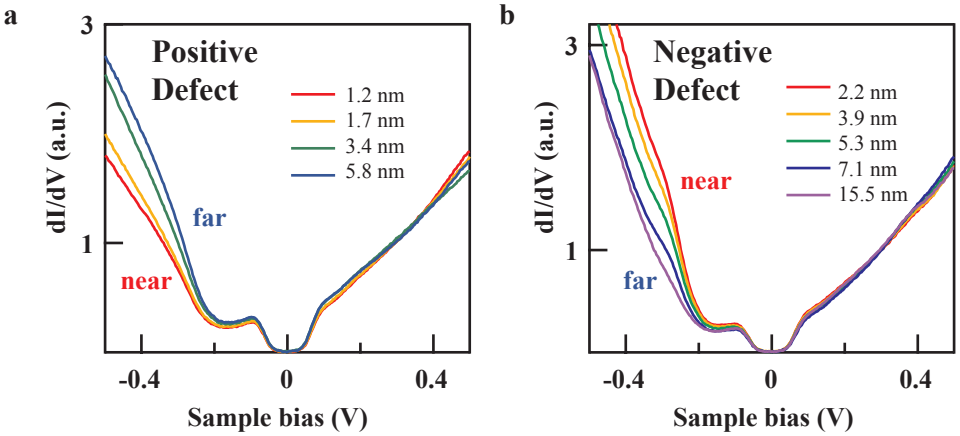

Supplementary Figure S7

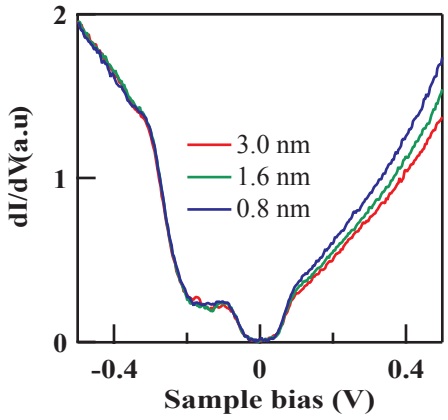

Supplementary Figure S8

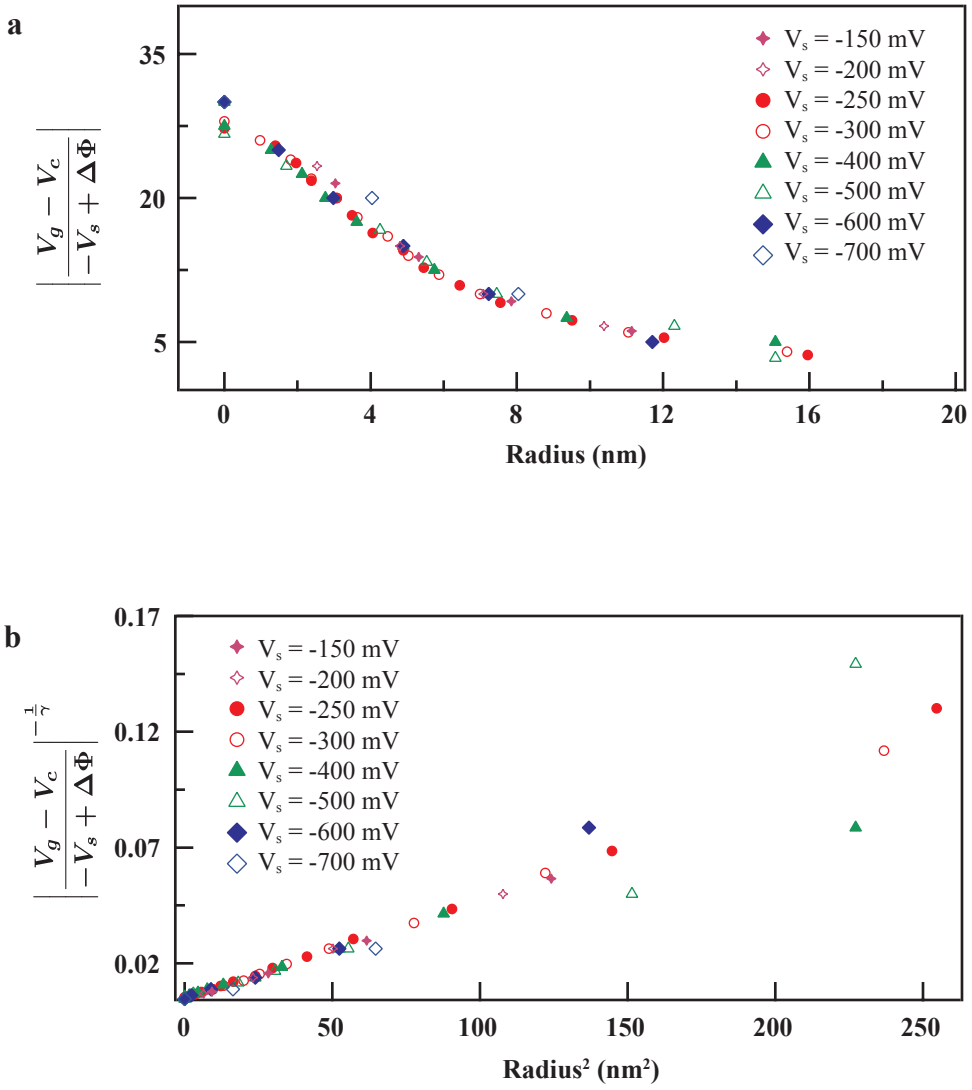

Supplementary Figure S9